ACS APPLIED MATERIALS & INTERFACES

Research Article

www.acsami.org

Scalable Synthesis of Urchin- and Flowerlike Hierarchical NiO Microspheres and Their Electrochemical Property for Lithium Storage

Jia Hong Pan, Qizhao Huang, Zhen Yu Koh, Darren Neo, Xing Zhu Wang, and Qing Wang*

Department of Materials Science and Engineering, Faculty of Engineering, NUSNNI-NanoCore, National University of Singapore, Singapore 117576

Supporting Information

ABSTRACT: A nickel salt−urea−H_2O ternary system has been developed for the large-scale synthesis of hierarchical α-$Ni(OH)_2$ microspheres, the solid precursor for the subsequent topotactic transition to NiO upon calcination. In this facile synthetic system, hierarchical structure is self-assembled under the cooperative direction of urea and anions in nickel salts. Thus, simply tuning the Ni salts leads to the selective construction of urchin and flowerlike hierarchical α-$Ni(OH)_2$ and NiO microspheres consisting of radial 1D nanowires and 2D nanoplates, respectively. The obtained NiO microspheres possessing accessible nanopores, excellent structural stability and large surface area up to 130 m^2/g show promising electrochemical performance in anodic lithium storage for lithium-ion battery.

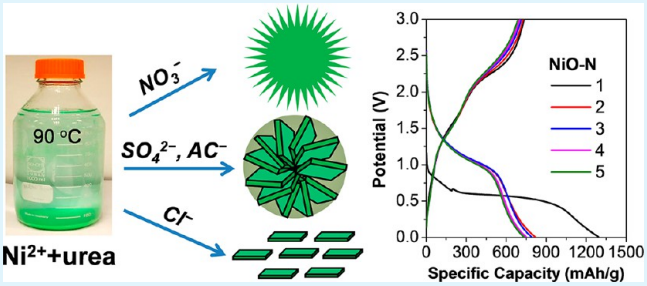

KEYWORDS: *NiO, X-ray diffraction, self-assembly, porous structure, chemical solution process, lithium-ion battery*

1. INTRODUCTION

Self-assembly has been a practical strategy to facilely tailor ensembles of nanostructures.[1] Three-dimensional (3D) urchin-like or flowerlike spherical architecture consisting of one-dimensional (1D) nanowires or two-dimensional (2D) nanoflakes via the oriented attachment is one of the representative self-assembled morphologies, which has also been widely found in naturally inorganic materials, such as $CaCO_3$, metal hydroxides, metal oxides, and zeolites.[2−4] Up to now artificial, self-assembly has been extensively explored as a versatile approach for designing hierarchical structures for metal oxides, sulfides, phosphate, and so forth.[5,6] Many studies have demonstrated that the synthesized superstructured materials possess favorable merits.[7−11] For instance, their structural diversity at nano- and microscales leads to a synergistic effect on improving the material properties because of the presence of well-defined and accessible voids among organized nanobuilding blocks (NBBs). On the other hand, their structural stability is significantly enhanced since the nanosized components are integrated in the large and thermodynamically stable spheres.

Nickel(II) oxide (NiO) has attracted great interest because of its favorable physicochemical properties for a broad range of applications, such as photovoltaics,[12,13] batteries,[14] (photo)-catalysis,[15] gas sensors,[16] absorbents,[17−19] and electrochromic windows.[20] In particular, recent progress has demonstrated that NiO is an interesting anode material for lithium-ion battery (LIB) to deliver ultrahigh capacity.[21−24] Exploring facile and scalable synthetic strategies for the preparation of nanostructured NiO is of great importance since the performance of the fabricated LIB is closely related to the electrochemical activity and structural stability of the material. Conventional gas phase-based synthetic methods such as flame synthesis have been developed as a dry route to NiO nanoparticles.[25,26] Alternatively, wet chemical route has been proposed as a facile and cost-effective procedure for the controllable synthesis of NiO. The synthetic method is mainly based on the indiscriminate precipitation of insoluble nanostructured intermediates (e.g., $Ni(OH)_2$) in the presence of strong alkaline (e.g., NaOH, KOH, or NH_3).[27−31] Upon calcination, a topotactic transition to NiO can be induced. Therefore, as a result of the monoclinic or brucite crystallographical structures of $Ni(OH)_2$, the obtained NiO nanomaterials are mostly in 1D or 2D forms of plate, fiber, or ribbon. These low-dimensional NiO materials are unfortunately not ideal for LIB despite their great structural versatility. They are prone to agglomeration upon continuous charge/discharge, eventually giving rise to significant capacity loss. To improve the performance stability, hierarchical NiO spheres derived from the self-assembly of low-dimensional and nanosized NiO have thus attracted increasing interest. Hydro/solvothermal process has been generally applied to compel the nucleation, crystal growth and self-

Received: April 11, 2013
Accepted: June 10, 2013
Published: June 10, 2013

assembly of nickel precursors under critical conditions.[32] Here the use of organic compounds such as organic solvents,[33,34] surfactants,[35−37] and chelants[17,38] have been widely present in the nickel source solutions to aid the self-assembly process and to facilitate the morphological control.

From a practical point of view, developing a mild, high-yield, and cost-effective process without using high pressure and temperature, toxic agents, and complex apparatus remains an urgent challenge. In line with the aim of a green and scalable synthesis, we report a chemical solution process capable of the large-scale synthesis of α-$Ni(OH)_2$ and NiO with hierarchical superstructures. The preparation is carried out in a nickel salt−urea−H_2O ternary system. By simply changing to different nickel salts, various 3-D hierarchical NiO microspheres consisting of 1D nanowires, or 2D nanoplates can be selectively synthesized. These hierarchical NiO microspheres with tunable NBBs offer an excellent platform to study the influence of NiO microstructures on their electrochemical performance. To the best of our knowledge, this is the first report for the mass production and controllable synthesis of large-surface-area hierarchical architectures for NiO and α-$Ni(OH)_2$.

2. EXPERIMENTAL SECTION

2.1. Preparation of Hierarchical NiO Microspheres. All chemicals were purchased from Aldrich without further purification. Mass production of hierarchical NiO microspheres was carried out in a 1 L Schott Duran glass bottle with a polypropylene screw cap (see the inset of Figure 1a). $Ni(NO_3)_2$ (nickel(II) nitrate hexahydrate), $Ni(SO_4)_2$ (nickel(II) sulfate hexahydrate, 99%), $NiCl_2$ (nickel(II) chloride, 98%), and $Ni(Ac)_2$ (nickel(II) acetate tetrahydrate, ≥98%) were used as nickel sources. Typically, nickel salt and urea were readily mixed in 900 mL water. The concentration of nickel salt and urea was fixed at 0.06 and 0.30 mol/L, respectively. The glass bottle was sealed and kept statically in an oven at 90 °C for 18 h. After reaction, the bottle was then cooled naturally down to room temperature, and the green α-$Ni(OH)_2$ precipitates were centrifuged and washed with water. Finally, NiO was obtained by calcining α-$Ni(OH)_2$ in air at 500 °C for 2 h. We denoted α-$Ni(OH)_2$ and NiO derived from different nickel sources as α-$Ni(OH)_2$-X and NiO-X, where X is N, S, Cl ,or Ac, standing for nickel source with different anions of NO_3^-, SO_4^{2-}, Cl^-, and acetate (Ac^-), respectively.

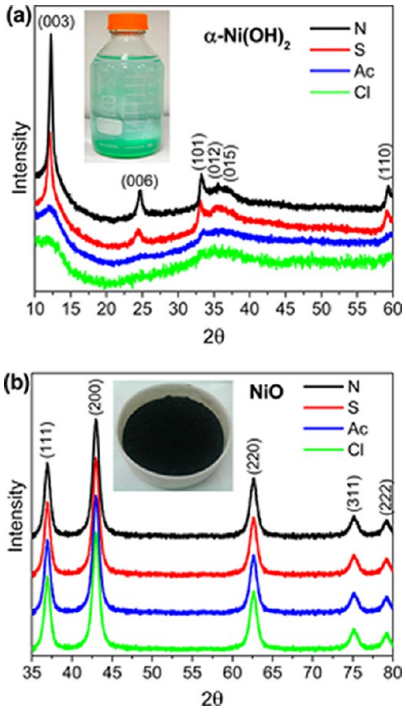

Figure 1. (a) Wide-angle XRD patterns of α-$Ni(OH)_2$ and (b) the resultant NiO synthesized from the solution process using nickel sources of $Ni(NO_3)_2$ (-N), $NiSO_4$ (-S), $NiCl_2$ (-Cl), and $Ni(Ac)_2$ (-Ac). The insets show the digital photographs of the related products.

2.2. Materials Characterization. X-ray diffraction (XRD) patterns were obtained using a Bruker D8 Advance X-ray diffractometer with a monochromated high-intensity CuKα radiation of wavelength λ = 0.15418 nm. Samples were scanned under ambient conditions. Thermogravimetry (TG) and differential scanning calorimetry (DSC) measurements were performed in air with a heating rate of 10 °C/min using a SDT Q600 V8.0 Build 95 thermoanalytical apparatus. The morphology and surface microstructure of NiO were observed by a Zeiss Supra 40 field-effect scanning electron microscope (SEM) and a JEOL JEM-2010 transmission electron microscope (TEM). Nitrogen (N_2) adsorption−desorption isotherms were obtained using a surface area and porosimetry analyzer (Nova 1000, Quantachrome Instruments). Before measurement, 0.1−0.2 g NiO samples were outgassed under vacuum for 8 h at 200 °C. Brunauer−Emmett−Teller (BET) equation was used to calculate the surface area from adsorption data obtained at P/P_0 = 0.01−0.30. The average pore diameter was estimated using the Barrett−Joyner−Halenda (BJH) method from the adsorption branch of the isotherm. The total volume of mesopores was calculated from the amount of N_2 adsorbed at P/P_0 = 0.975−0.977, assuming that adsorption on the external surface was negligible compared to adsorption in pores.

2.3. Electrochemical Characterization. Hierarchical NiO microspheres, carbon black and polyvinylidene difluoride (PVDF) binder were mixed thoroughly at a weight ratio of 8:1:1 in *N*-methylpyrrolidone (NMP). The formed viscous slurry was doctor bladed on Cu foil and then dried in vacuum at 120 °C for 18 h. The weight of the dried working anode was ~6 mg/cm^2. Lithium foil was used as both the counter and the reference electrodes. 1.0 mol/L $LiPF_6$ in a solution of ethylene carbonate (EC) and diethyl carbonate (DEC) at a volume ratio of 1:1 was used as the electrolyte. Electrochemical measurements were carried out at room temperature. Cyclic voltammetry (CV) measurements were performed on an Autolab PGSTAT100 at a scanning rate of 0.5 mV/s. Galvanostatic charge and discharge measurements were carried out in the voltage range of 0.01−3.0 V at a current density of 50 mA/g. For comparison, commercially available NiO nanoparticles (NiO-NPs, < 50 nm) were also tested at identical conditions.

3. RESULTS AND DISSCUSSION

3.1. Characterization of Hierarchical NiO Microspheres. XRD analysis was carried out to identify the crystal structure, composition, and orientation of α-$Ni(OH)_2$ precipitated from the chemical solution. As shown in Figure 1a, the wide-angle XRD peak positions for all the four samples are matched well with the hexagonal α-$Ni(OH)_2{\cdot}0.75H_2O$ phase (ICDD No. card 38−0715) with the lattice parameters a = 3.08 Å and c = 23.41 Å. Because of the weakly alkaline medium created by stepwise hydrolysis of urea, β-$Ni(OH)_2$ phase, which is generally synthesized from a high pH condition, is not observed.

Although different Ni sources are found to form an identical crystal phase, slight shifts occur in the diffraction peaks, which can be ascribed to the different anions intercalated in the α-$Ni(OH)_2$ lattice.[39] Moreover, the presence of anions in the aqueous solution seems to affect the crystallization of α-$Ni(OH)_2$. Significant differences in the relative intensity of each diffraction peak can be observed. Taking the predominant (003) peak at 2θ of 12−14° as a reference, a strong and sharp diffraction peak is found in α-$Ni(OH)_2$-N or -S, while α-

dx.doi.org/10.1021/am401330g | ACS Appl. Mater. Interfaces 2013, 5, 6292−6299

Table 1. Textural Properties of NiO Synthesized Using Different Nickel Salts

sample	Ni source	yield (%)	morphology	NBBs[a]	S_{BET} (m^2/g)[b]	D_p (nm)[c]	V_p (cm^3/g)[d]
NiO-N	$Ni(NO_3)_2$	94	microsphere	nanowires	113.3	5.4	0.209
NiO-S	$NiSO_4$	96	microsphere	nanoplates	130.2	5.0	0.163
NiO-Ac	Ni $(Ac)_2$	90	microsphere	nanoplates	102.8	8.7	0.152
NiO-Cl	$NiCl_2$	87	nanoplate		81.6	9.1	0.148

[a]Nanobuilding blocks. [b]BET surface area. [c]Pore size. [d]Pore volume.

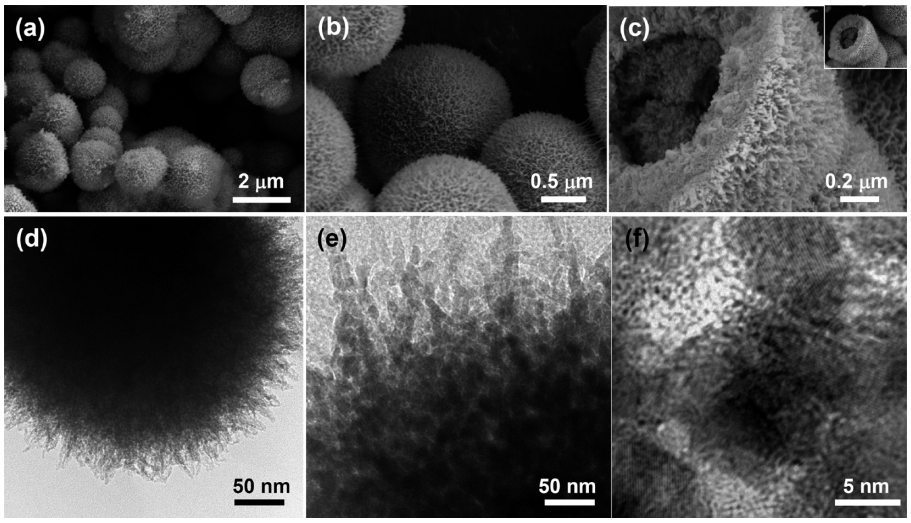

Figure 2. (a–c) SEM, (d, e) TEM, and (f) high-resolution TEM images of urchinlike hierarchical NiO-N microspheres consisting of radial nanowires.

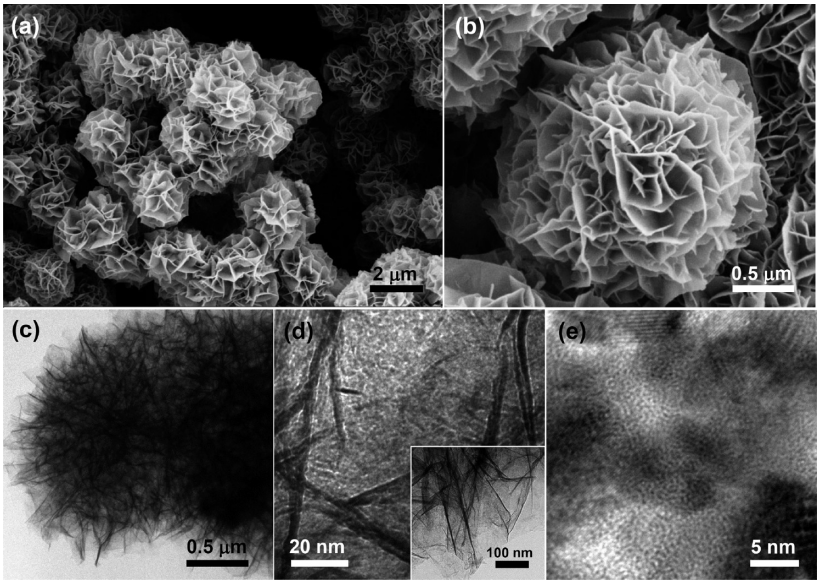

Figure 3. (a, b) SEM, (c, d) TEM, and (e) high-resolution TEM images of flowerlike hierarchical NiO-S microspheres consisting of interconnected nanoplates.

$Ni(OH)_2$-Ac or −Cl merely shows a broad and weak peak. This result suggests that a preferential growth of α-$Ni(OH)_2$ along the (001) plane in the presence of SO_4^{2-} and NO_3^-.

Upon calcination, α-$Ni(OH)_2$ was converted into NiO. The obtained NiO samples were all in black color (inset of Figure 1b) because of the presence of Ni vacancies, indicating their nonstoichiometric ($Ni_{1-x}O$) nature.[40] Figure 1b shows their wide-angle XRD patterns. All the NiO samples display a similar face-centered cubic (FCC with a lattice parameter a = 4.18 Å) NiO phase (ICDD No. 71–1179) without any impurity peaks.

TGA analysis was used to further monitor the underlying phase transformation from α-$Ni(OH)_2$ to NiO. Figure S1 in the Supporting Information shows the TGA and DSC curves of α-$Ni(OH)_2$-S with temperature increments from 30 to 800 °C. The weight loss between 100 and 200 °C can be attributed primarily to the release of residual and adsorbed water, along with the dissociation of a small amount of intercalated species

(e.g., H_2O and NH_3) or adsorbed anions. A sharp weight loss of ~19.6% at the temperature range of 250−350 °C was observed, which is close to the theoretical value of 19.4% for the complete thermal pyrolysis of α-$Ni(OH)_2$ to NiO with the release of isometric water steam. The excess weight loss may be attributed to the removal of the intercalated anions (NO_3^-, SO_4^{2-}, Cl^-, or Ac^-). As further confirmed by the DSC curve, a strong endothermic peak can be observed around 380 °C. Beyond that temperature, no distinct weight loss presents, indicating that the resultant FCC NiO phase shows an excellent thermal stability at high temperatures.

Table 1 summarizes the structural and pore characteristics of the synthesized four NiO samples. Dependent on the nickel precursor used, the resultant NiO materials exhibit distinct morphology and microstructure. All the samples are microspherical except that NiO-Cl is in the form of nanoplates. NiO-N, -S, and -Ac are significantly different in diameter and shape of NBBs. NiO-N displays an urchinlike structure consisting of nanowire NBBs, whereas NiO-S and -Ac are flowerlike microspheres built up by nanoplates.

Urchinlike NiO-N microspheres with an almost 100% morphological yield were synthesized by using $Ni(NO_3)_2$ as the Ni source. Figure 2 depicts their morphology and microstructure revealed by SEM and TEM. NiO-N microspheres are monodisperse with diameters ranging from 1.0 to 2.5 μm (Figure 2a). A number of radially arranged nanowires emanates from the spherical surface (Figure 2b). A broken sphere shown in Figure 2c and Figure S2 in the Supporting Information clearly suggests that the nanowires have a uniform length of around 100 nm. Images d and e in Figure 2 show their corresponding TEM images, in which each nanowire consists of closely attached nanocrystallites. The high-resolution TEM image in Figure 2f shows the lattice fringes of the nanocrystallite with a *d*-spacing of 3.5 Å, which can be assigned to the (101) plane of NiO.

Flowerlike NiO-S microspheres were derived from a $NiSO_4$−urea−H_2O system. Similar to NiO-N, NiO-S also possesses a monodisperse spherical morphology with diameters ranging from 1−3 μm, observed from the SEM images in Figure 3a, b. The hierarchical superstructure is built from the intersectional rhombohedral nanoplates with a mean edge length of about 500−800 nm and a uniform thickness of about 50 nm. The hierarchical superstructure is further revealed by TEM. Images c and d in Figure 3 clearly show that the spheres are assembled by nanosheets with a uniform thickness of ca. 3.6 nm, and numerous tiny pores present on the flat lamina due to the release of H_2O and the structural contraction during calcination process.[41] A high-resolution TEM image shown in Figure 3e exhibits the crystal lattices of a single nanosheet, which is composed of closely packed NiO nanocrystallites surrounding the pores. The (101) crystal planes with a *d*-spacing of 3.5 Å can be clearly observed on each nanocrystallite, indicating the polycrystalline nature of the nanoplates.

Panels a and b in Figure 4 show the representative SEM images of NiO-Ac and NiO-Cl, respectively. NiO-Ac has a similar flowerlike morphology to NiO-S with a diameter of 0.9−1.2 μm. However, NiO-Ac reveals a relatively low degree in self-assembly of nanoplates, where only a few nanoplates with a larger thickness of 100−200 nm are present in the microspheres. Interestingly, the lowest assembly was found in NiO-Cl among the four samples, where merely isolated nanoplates with sizes around 0.3 μm are observed.

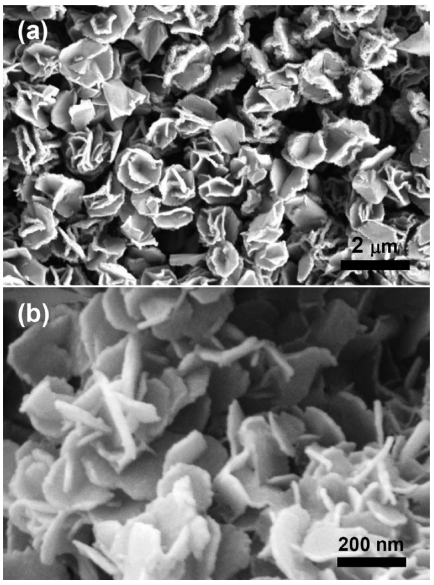

Figure 4. SEM images of (a) hierarchical NiO-Ac microspheres and (b) NiO-Cl nanoplates.

N_2 adsorption−desorption isotherms and the related pore diameter distribution have been measured to further elucidate the hierarchical structure in NiO. As shown in Figure 5a, all the

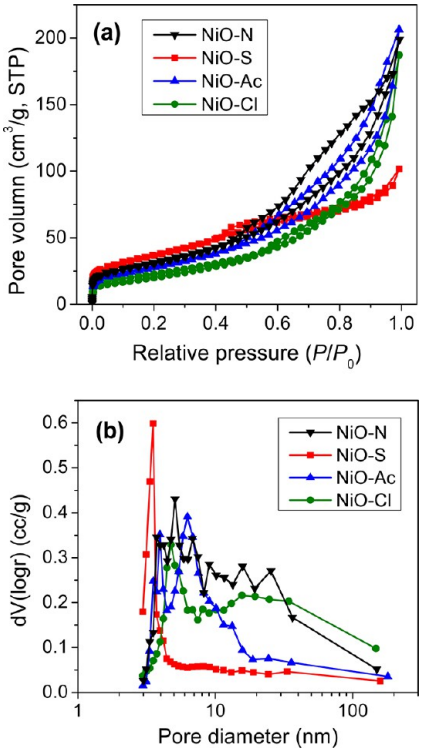

Figure 5. (a) N_2 adsorption−desorption isotherms and (b) pore size distribution plots for NiO nanomaterials using different nickel sources.

synthesized NiO exhibit type-IV isotherm plots with a sharp capillary condensation steps, indicative of mesoporous structures. Typically, the BET surface areas of NiO-S and NiO-N are 130.2 and 113.3 m^2/g, respectively, which are about two times higher than that of the commercial NiO nanoparticles (43.0 m^2/g). The great improvements in specific

dx.doi.org/10.1021/am401330g | ACS Appl. Mater. Interfaces 2013, 5, 6292−6299

surface area may arise from the voids among close-packing NBBs, and the mesopores in the nanoplates or nanowires. In contrast to NiO-N and -S, NiO-Ac and -Cl have relatively smaller surface area. This result is consistent with their downgraded hierarchical structure caused by the lower degree of self-assembly. Figure 5b shows the pore size distributions for all NiO samples, where narrow pore size distributions with an average pore diameter less than 10 nm are generally observed. These small mesopores are likely originated from the mesoporous voids between the nanocrystallites.

3.2. Formation Mechanism of Hierarchical Structures. The ultimate morphologies of NiO are derived from the topotactic transition of α-$Ni(OH)_2$ by thermal pyrolysis, and α-$Ni(OH)_2$ is obtained by free precipitation from a solution reaction at 90 °C. In this mild temperature, urea hydrolyzes gradually and releases NH_3 and CO_2. The resulting weak alkaline condition is believed to create numerous nucleation sites for the formation of supersaturated α-$Ni(OH)_2$ nanoplates, whereas the growth of α-$Ni(OH)_2$ is suppressed, which affords sufficient time for the spontaneous self-assembly of these nanosized α-$Ni(OH)_2$, leading to the oriented stacking of nanoflakes perpendicular to the (003) plane to minimize their mutual interaction energy.[41] α-$Ni(OH)_2$ microspheres are formed and precipitate out from the solution upon 0D to 2D nucleation−growth and the subsequent 3D self-assembly. The related reaction formulas can be written as follows.

$$CO(NH_2)_2 + H_2O \rightarrow 2NH_3 + CO_2 \quad (1)$$

$$Ni^{2+} + 2NH_3 + 2H_2O \rightarrow \alpha - Ni(OH)_2 + 2NH_4^+ \quad (2)$$

The self-assembly process of α-$Ni(OH)_2$ was proved by monitoring the continuous morphological evolutions of α-$Ni(OH)_2$. Green precipitates were collected at different time intervals for SEM measurement. After reacting for 3 h, α-$Ni(OH)_2$ started to precipitate. As revealed by SEM analysis in Figure S3 in the Supporting Information, a number of flowerlike microspheres consisting of nanoplates was formed in all the pristine precipitations of α-$Ni(OH)_2$-S, -Ac, and -N. It is pronounced that the self-assembly process occurs in the homogeneous solutions with the formation of hierarchical structure before precipitation. The driving forces of self-assembly can be considered to be electrostatic repulsive forces, van der Waals attractive forces, hydrogen bonding, steric forces, and hydrophobic−hydrophobic interactions.[8] With further increasing the reaction time, the yield and the size of α-$Ni(OH)_2$ were gradually increased. For α-$Ni(OH)_2$-S and -Ac, their flowerlike morphology of remained unchanged. Apparently, self-assembly of NBBs has almost finished in the supersaturated solution. The pristine flowerlike α-$Ni(OH)_2$ spheres, i.e., as-formed precipitates, can grow further by simply harvesting the unreacted species on their surface.

Unlike α-$Ni(OH)_2$-S and -Ac, a secondary growth takes place in the primary flowerlike α-Ni(OH)-N frameworks, which induces a morphological transformation in NBBs from nanoplate to nanowire. At 8 h, nanowires appeared on the surface of nanoplates, and an urchinlike superstructure with radial nanowires was reconstructed, as shown in Figure S4 in the Supporting Information. Thus, it can be concluded that the unique nanowire NBBs in α-$Ni(OH)_2$-N are due to the secondary growth of the flowerlike structure. Indeed, Figure 2c and Figure S2 in the Supporting Information have shown that the interior of NiO-N contains aggregated nanoplates, although the outer spherical surface comprises radial nanowires.

The capability of tuning NiO superstructures by simply using different nickel sources is one of the most striking features of our currently developed synthetic strategy. The selective control of morphology relies on the existence of anions in the employed nickel salts. Then how do anions determine the morphology of product and structure of NBBs? During chemical solution reaction, anions are able to tune the crystal growth and self-assembly of α-$Ni(OH)_2$ by grafting preferentially to its particular crystal facet via adsorption or intercalation. Their different anionic nature (size, hydrophilicity, net charges) and coordination ability have a great influence on the crystal growth and self-assembly of α-$Ni(OH)_2$.

Compared with inorganic anions, larger-sized Ac^- ions with less hydrophilicity may impede the mobility of OH^- ions toward the surface of α-$Ni(OH)_2$ sheets to a greater extent,[42] guiding a lower-degree self-assembly and a lower crystallinity of α-$Ni(OH)_2$-Ac. Therefore, as can be seen in Figure 1a, it is not surprising that α-$Ni(OH)_2$-Ac shows a much weaker diffraction in its XRD patterns, in comparison with α-$Ni(OH)_2$-N and -S.

With the hydrolysis of urea, the created supersaturated condition drives a preferential crystal growth of α-$Ni(OH)_2$ along the (100) and (010) direction to minimize the surface energy and electrostatic repulsion. Primary nanoflakes are formed for α-$Ni(OH)_2$-N and others. They will then self-assemble to complete the stabilization. The flowerlike spheres consisting of nanoflakes are thus readily precipitated from the solution, and can attract reactants for further growth. Free NO_3^- show the lowest affinity on the interlayers of α-$Ni(OH)_2$, among the anions introduced from nickel sources, and even lower than OH^-.[43] Thus, α-$Ni(OH)_2$-N may prefer to adsorb and intercalate OH^-. The rich OH^- on the α-$Ni(OH)_2$-N surface seems to guide an anisotropy crystal growth that is entirely different from the NO_3^--rich chemical solution reaction. In contrast, SO_4^{2-} ions show a much higher affinity on α-$Ni(OH)_2$-S than OH^-. The presence of large-sized SO_4^{2-} in the interlayer decreases the OH^- intercalation, guiding the continuous growth of nanoflakes.

Self-assembly process did not operate in the $NiCl_2$-containing system. Presumably, smallest-sized Cl^- ions with a prominent complexing ability can be easily grafted on the α-$Ni(OH)_2$ nuclei and lower their surface energy. Primary α-$Ni(OH)_2$-Cl tends to be thermodynamically stable, which hinders the subsequent self-assembly process. Consequently, free nanoflakes rather than aggregates are precipitated from the supersaturated solution. The formed α-$Ni(OH)_2$-Cl with rich intercalated Cl^- ions shows a low crystallinity, as revealed by XRD analysis in Figure 1a.

We then investigated the role of urea in the self-assembly process. As can be seen from the reactions 1 and 2, the stoichiometric molar ratio of urea and Ni source (R_u) is 1:1 during the course of the formation of α-$Ni(OH)_2$. However, at this condition, no precipitation occurred for all four nickel sources after 18 h reaction at 90 °C, probably due to the slow reaction dynamics. Irregular shapes were found in NiO products when adjusting R_u to 3:1. Hence, an excessive urea is critical to the synthesis of hierarchical NiO microspheres, and the minimal value for R_u is found to be 5:1.

Apparently, a high dosage of urea is corresponding to a high concentration of OH^- ions in the aqueous medium during chemical solution reaction. With the stepwise hydrolysis of urea, α-$Ni(OH)_2$ nuclei are formed, and the excessive free OH^- species can be subsequently adsorbed on the their Ni^{2+}

exposing facets, which enhances the polarity of negatively charged α-Ni(OH)$_2$. As a result, the interactions between these dipoles lead to the 3D self-assembly with the assistances of electrostatic forces and hydrogen bonding. Therefore, urea acts not only as a mineralizing agent to induce the formation and crystal growth of α-Ni(OH)$_2$, but also as a morphology controller to mediate the self-assembly of α-Ni(OH)$_2$ superstructures.

Attempts have also been made to investigate the effect of the reaction conditions on the morphology of NiO. Interestingly, static reaction system was found to be critical to form the hierarchical structures. Control experiments were carried out by stirring the solution in an oil bath at 90 °C but keeping other conditions constant. The resultant α-Ni(OH)$_2$-N and -Ac were mainly in the form of isolated nanoplates (see Figure S5 in the Supporting Information). Apparently, the mechanical agitation significantly disturbs the self-assembly of NBBs. On the contrary, no noticeable morphological alteration was found in α-Ni(OH)$_2$-S samples. These results further validate our speculation that electrostatic attractive force mediates in the self-assembly process because SO_4^{2-} holds the highest ionic strength in the aqueous solution.

3.3. Electrochemical Characterizations. The obtained NiO microspheres possessing large surface area and hierarchical structure are intriguing for LIB applications. We selected NiO-N and NiO-S, along with the commercial NiO-NPs to evaluate their electrochemical properties in lithium half-cells. Figure S6 in the Supporting Information shows the CV curves of NiO-NPs, NiO-S, and NiO-N tested over voltage range from 0.01 to 3.0 V at a scanning rate of 0.5 mV/s. All the NiO anodes show similar redox reactions during lithium insertion and extraction processes. The representative first five CV curves of NiO-N are shown in Figure 6. In the first cycle, an intensive reduction peak

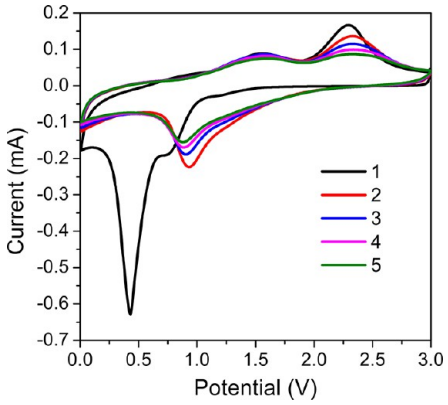

Figure 6. The first five cycles CVs for the electrodes made of NiO-N microspheres. The electrolyte was 1.0 M $LiPF_6$ in EC+DEC (1:1). The scan rate was 0.5 mV/s.

centered at 0.43 V and a shoulder at around 0.74 V appear, corresponding respectively to the formation of a partially reversible solid electrolyte interface (SEI) layer and the initial reduction of NiO to metallic Ni nanoparticles according to eq 3 below.[29]

$$NiO + 2Li^+ + 2e^- \rightarrow Ni + Li_2O \quad (3)$$

Subsequently, the in situ formed metallic Ni phase restores and releases Li ions during the oxidation process

$$Ni + Li_2O \leftrightarrow NiO + 2Li^+ + 2e^- \quad (4)$$

As can be clearly seen in the CV curves, an oxidation peak at 2.30 V and a relatively broader peak at 1.56 V can be resolved, which can be ascribed to the reversible oxidation of Ni (eq 4) and the partial decomposition of SEI layer, respectively.

In the second cycle, the main peaks become broad with remarkably decreased peak current. In addition, the reduction peak shifts to a higher potential of 0.93 V, indicating the microstructure of NiO has undergone substantial changes after Li insertion and extraction during the first cycle. This microstructural evolution accompanies significant capacity loss due to the irreversible formation and decomposition of Li_2O and SEI layer. This irreversibility is highly related to the size, dimension, and microstructure of NiO, as widely found in other binary transition metal oxide-based LIB anodes.[21,24]

The voltage−specific capacity profiles of the NiO-based half cells were obtained at a constant current density of 50 mA/g. Figure 7 shows the charge−discharge curves of NiO-N, NiO-S, and NiO-NPs in the first 5 cycles at a scan rate of 0.2 C. The NiO-N and NiO-S have ultrahigh initial capacities of 1295 and

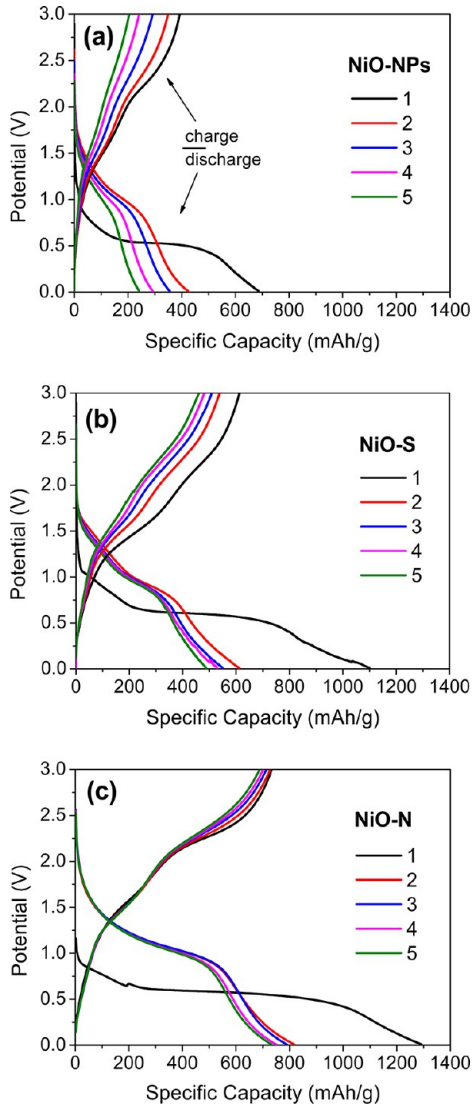

Figure 7. Galvanostatic charge/discharge curves of (a) NiO-NPs, (b) NiO-S, and (c) NiO-N tested in Li-half cells. The electrolyte was 1.0 M $LiPF_6$ in EC+DEC (1:1). The current density was 50 mA/g, and the scan rate was 0.2C.

dx.doi.org/10.1021/am401330g | ACS Appl. Mater. Interfaces 2013, 5, 6292−6299

1104 mA h/g, respectively, far greater than that of the NiO-NPs (824 mA h/g). All these initial capacities are higher than the theoretical capacity (718 mA h/g) for bulk NiO.[29] The exceeded capacity is as a result of large surface area, originating from the formed SEI layer during the first reduction.[44] In the subsequent cycles, the capacities of NiO-S and NiO-NPs decrease continuously because of the kinetic restrictions associated with the incomplete decomposition of Li_2O and continuous formation of SEI. After 5 cycles, NiO-S has a reversible capacity of 491 mA h/g, whereas that of NiO-NP is only 243 mA h/g. In contrast, NiO-N delivers a much greater capacity retention. The capacity of 739 mA h/g after 5 cycles is actually largely stabilized from the second cycle, suggesting a close correlation between reversible lithium insertion/extraction and microstructures of the materials. The enhanced performance of NiO-N is presumably ascribed to (1) the hierarchical structure being more accessible for electrolyte diffusion and Li^+ insertion/extraction; (2) the well-defined superstructure prohibiting the aggregation of Ni nanocrystallites, relieving the structural stress induced by volume changes during the charge−discharge cycles, and thereby suppressing the degradation of the NiO electrode; (3) the large surface area offering more active sites for the "conversion reaction", which on the other hand gives rise to large irreversible capacity loss; (4) the unique NBBs, especially 1D nanowires with fewer grain boundaries being more favorable for faster Li^+ diffusion, compared with 2D nanoflakes consisting of numerous nanocrystallites.[45]

To further reveal their stabilities in electrochemical performances, we measured cyclic performances of LIB anodes based on NiO-S and NiO-N microspheres, and their discharge and charge capacities for each cycle at different scanning speeds of 0.2 and 0.5 C are plotted in Figure S7a, b in the Supporting Information, respectively. With the proceeding of the cyclic discharge−charge, the charge−discharge capacity is gradually faded, while the irreversible capacity is decreased. After 30 cycles, the values of NiO-S electrode are significantly decreased to 117 and 105 mA h/g at 0.2 *C* and 97.7 and 84.2 mA h/g at 0.5 *C*, respectively, which are in good agreement with the results from Liu et al.[37] In contrast, the NiO-N anode exhibits a better cycle performance and their stabilized discharge−charge capacities after 50 cycles are as high as 163 and 134 mA h/g at 0.2 *C* and 116.0 and 102.5 mA h/g.

The different stability in capacity output of NiO-N and NiO-S is resulted from their extreme diversity in the structure and organization of NBBs. To understand how the degradation of morphology is corresponding to the capacity retention, we compared the morphology between NiO-N and NiO-S after 30 charge−discharge cycles at a scan rate of 0.2 *C*. As shown in Figure S8 in the Supporting Information, a well-resolved spherical structure remains in NiO-N, whereas NiO-S is almost distorted and small crystallites and bulk structure are dominated. For both samples, nanoparticles present on their surface because of the redox reactions according to eqs 3 and 4. During a cyclic discharge−charge process, the highly open framework of NiO-S consisting of the mutually supported ultrathin nanoplates are supposed to present an over high accessibility for Li^+ and electrolyte. NiO nanocrystallines in nanoflakes are subjected to the intensive redox reactions. They are easy to isolate from the thin nanoflakes, leading to the serious distortion of the mother hierarchical structure. Comparably, NiO-N anode reserves its transport advantages due to the orientational packing of nanowires in the interiors and long nanowires in the exteriors. Its relatively closer spherical structure with higher structural stability would be able to deliver a stable cyclic performance.

4. CONCLUSIONS

In summary, we have developed a facile chemical solution method for the mass production of hierarchical microspheres of α-$Ni(OH)_2$ and the resultant NiO. By simply tuning the nickel salt in the nickel salt−urea−H_2O ternary system, urchin, and flowerlike hierarchical microspheres can be selectively self-assembled with the assistance of urea as the directing agent. Anions intercalated in the crystal lattices of α-$Ni(OH)_2$ are found to have a great influence of the self-assembly process and hence determine the morphology and microstructure of α-$Ni(OH)_2$ and NiO. The synthesized hierarchical NiO microspheres have high porosity and unique microstructures, which render promising electrochemical properties for lithium storage. The structure of NBBs shows significant influence on the discharge−charge capacity and stability, and nanowire NBBs show a relatively higher performance than nanoflakes. It is anticipated that the synthesized α-$Ni(OH)_2$ and NiO microspheres with the innate NBBs and large surface area may find other important applications for photocatalysis, photocathodes for sensitized photoelectrochemical cells, supercapacitor, etc.

■ ASSOCIATED CONTENT

Ⓢ Supporting Information

Figures S1−S8 showing DSC-TG curves and SEM micrographs of α-$Ni(OH)_2$, and SEM, CV curves, and cycle performances of different NiO samples. This materials is available free of charge via the Internet at http://pubs.acs.org/.

■ AUTHOR INFORMATION

Corresponding Author

*E-mail: msewq@nus.edu.sg. Tel: +65 6516-7118. Fax: +65 6776-3604.

Author Contributions

The manuscript was written through contributions of all authors. All authors have given approval to the final version of the manuscript.

Notes

The authors declare no competing financial interest.

■ ACKNOWLEDGMENTS

This research is supported by the National Research Foundation Singapore under its Competitive Research Program (CRP Award NRF-CRP8−2011−04) and NUS-FOE Energy Research for Sustainability Initiatives (R284000089112).

■ REFERENCES

(1) Meldrum, F. C.; Colfen, H. *Chem. Rev.* **2008**, *108*, 4332−4432.
(2) Dickerson, M. B.; Sandhage, K. H.; Naik, R. R. *Chem. Rev.* **2008**, *108*, 4935−4978.
(3) Palmer, L. C.; Newcomb, C. J.; Kaltz, S. R.; Spoerke, E. D.; Stupp, S. I. *Chem. Rev.* **2008**, *108*, 4754−4783.
(4) Sommerdijk, N. A. J. M.; With, G. d. *Chem. Rev.* **2008**, *108*, 4499−4550.
(5) Sanchez, C.; Arribart, H.; Guille, M. M. G. *Nat. Mater.* **2005**, *4*, 277−288.
(6) Mann, S. *Nat. Mater.* **2009**, *8*, 781−792.
(7) Zhang, W.; Li, M.; Wang, Q.; Chen, G.; Kong, M.; Yang, Z.; Mann, S. *Adv. Funct. Mater.* **2011**, *21*, 3516−3523.

(8) Pan, J. H.; Dou, H.; Xiong, Z.; Xu, C.; Ma, J.; Zhao, X. S. *J. Mater. Chem.* **2010**, *20*, 4512−4528.
(9) Yec, C. C.; Zeng, H. C. *Chem. Mater.* **2012**, *24*, 1917−1929.
(10) Zhang, K.; Han, P.; Gu, L.; Zhang, L.; Liu, Z.; Kong, Q.; Zhang, C.; Dong, S.; Zhang, Z.; Yao, J.; Xu, H.; Cui, G.; Chen, L. *ACS Appl. Mater. Interfaces* **2012**, *4*, 658−664.
(11) Park, J. C.; Kim, J.; Kwon, H.; Song, H. *Adv. Mater.* **2009**, *21*, 803−807.
(12) Gibson, E. A.; Smeigh, A. L.; Le Pieux, L.; Fortage, J.; Boschloo, G.; Blart, E.; Pellegrin, Y.; Odobel, F.; Hagfeldt, A.; Hammarström, L. *Angew. Chem., Int. Ed.* **2009**, *48*, 4402−4405.
(13) Nattestad, A.; Mozer, A. J.; Fischer, M. K. R.; Cheng, Y. B.; Mishra, A.; Bäuerle, P.; Bach, U. *Nat. Mater.* **2010**, *9*, 31−35.
(14) Davar, F.; Fereshteh, Z.; Salavati-Niasari, M. *J. Alloys Compd.* **2009**, *476*, 797−801.
(15) Bai, G.; Dai, H.; Deng, J.; Liu, Y.; Ji, K. *Catal. Commun.* **2012**, *27*, 148−153.
(16) Cho, N. G.; Hwang, I.-S.; Kim, H.-G.; Lee, J.-H.; Kim, I.-D. *Sens. Actuators: B* **2011**, *155*, 366−371.
(17) Zhu, T.; Chen, J. S.; Lou, X. W. *J. Phys. Chem. C* **2012**, *116*, 6873−6878.
(18) Li, X.; Xiong, S.; Li, J.; Bai, J.; Qian, Y. *J. Mater. Chem.* **2012**, *22*, 14276−14283.
(19) Mahmood, T.; Saddique, M. T.; Naeem, A.; Mustafa, S.; Dilara, B.; Raza, Z. A. *J. Hazard. Mater.* **2011**, *185*, 824−828.
(20) Niklasson, G. A.; Granqvist, C. G. *J. Mater. Chem.* **2007**, *17*, 127−156.
(21) Poizot, P.; Laruelle, S.; Grugeon, S.; Dupont, L.; Tarascon, J. M. *Nature* **2000**, *407*, 496−499.
(22) Wang, X.; Li, X.; Sun, X.; Li, F.; Liu, Q.; Wang, Q.; He, D. *J. Mater. Chem.* **2011**, *21*, 3571−3573.
(23) Liu, H.; Wang, G.; Liu, J.; Qiao, S.; Ahn, H. *J. Mater. Chem.* **2011**, *21*, 3046−3052.
(24) Wu, H. B.; Chen, J. S.; Hng, H. H.; Wen Lou, X. *Nanoscale* **2012**, *4*, 2526−2542.
(25) Tricoli, A.; Righettoni, M.; Teleki, A. *Angew. Chem., Int. Ed.* **2010**, *49*, 7632−7659.
(26) Azurdia, J. A.; Marchal, J.; Shea, P.; Sun, H.; Pan, X. Q.; Laine, R. M. *Chem. Mater.* **2006**, *18*, 731−739.
(27) Peck, M. A.; Langell, M. A. *Chem. Mater.* **2012**, *24*, 4483−4490.
(28) Meneses, C. T.; Flores, W. H.; Garcia, F.; Sasaki, J. M. *J. Nanopart. Res.* **2007**, *9*, 501−505.
(29) Yuan, L.; Guo, Z. P.; Konstantinov, K.; Munroe, P.; Liu, H. K. *Electrochem. Solid-State Lett.* **2006**, *9*, A524−A528.
(30) Huang, Y.; Huang, X. L.; Lian, J. S.; Xu, D.; Wang, L. M.; Zhang, X. B. *J. Mater. Chem.* **2012**, *22*, 2844−2847.
(31) Mai, Y. J.; Tu, J. P.; Xia, X. H.; Gu, C. D.; Wang, X. L. *J. Power Sources* **2011**, *196*, 6388−6393.
(32) Dong, L.; Chu, Y.; Sun, W. *Chem.—Eur. J.* **2008**, *14*, 5064−5072.
(33) Dong, S.; Zhang, P.; Liu, H.; Li, N.; Huang, T. *Biosens. Bioelectron.* **2011**, *26*, 4082−4087.
(34) Chen, Y. C.; Zheng, F. C.; Min, Y. L.; Wang, T.; Wang, Y. X.; Zhang, Y. G. *Colloids Surf., A* **2012**, *395*, 125−130.
(35) Palanisamy, P.; Raichur, A. M. *Mater. Sci. Eng., C* **2009**, *29*, 199−204.
(36) Lee, J. W.; Ahn, T.; Kim, J. H.; Ko, J. M.; Kim, J.-D. *Electrochim. Acta* **2011**, *56*, 4849−4857.
(37) Liu, L.; Li, Y.; Yuan, S.; Ge, M.; Ren, M.; Sun, C.; Zhou, Z. *J. Phys. Chem. C* **2009**, *114*, 251−255.
(38) Chopra, N.; Claypoole, L.; Bachas, L. *J. Nanopart. Res.* **2010**, *12*, 2883−2893.
(39) Xu, L.; Ding, Y.-S.; Chen, C.-H.; Zhao, L.; Rimkus, C.; Joesten, R.; Suib, S. L. *Chem. Mater.* **2007**, *20*, 308−316.
(40) Fievet, F.; Germi, P.; de Bergevin, F.; Figlarz, M. *J. Appl. Crystallogr.* **1979**, *12*, 387−394.
(41) Pan, J. H.; Zhang, X.; Du, A. J.; Bai, H.; Ng, J.; Sun, D. *Phys. Chem. Chem. Phys.* **2012**, *14*, 7481−7489.
(42) Lee, J. W.; Ko, J. M.; Kim, J.-D. *J. Phys. Chem. C* **2011**, *115*, 19445−19454.
(43) Sun, D.; Zhang, J.; Ren, H.; Cui, Z.; Sun, D. *J. Phys. Chem. C* **2010**, *114*, 12110−12116.
(44) Huang, X. H.; Tu, J. P.; Zhang, C. Q.; Zhou, F. *Electrochim. Acta* **2010**, *55*, 8981−8985.
(45) Kavitha, T.; Yuvaraj, H. *J. Mater. Chem.* **2011**, *21*, 15686−15691.